Multilayered Graphene-Assisted Broadband Scattering Suppression through an Ultrathin and Ultralight Metasurface

Cheng Zhang,*,& Jie Zhao,& Bo Han Zhang, Rong Guo Song, Yu Chao Wang, Da Ping He,* and Qiang Cheng*

Read Online

ACCESS | Metrics & More | Article Recommendations | Supporting Information

ABSTRACT: Here, we present an ultralight multilayered graphene-based metasurface for suppressing specular reflection. With the help of a joint optimization method, dual low-reflection mechanisms including absorption and random diffusion are realized within the same structure, resulting in a remarkable decrease in the backward reflected energy in an ultrabroadband range of 7.5 to 43 GHz (a relative bandwidth of 140.6%). Experiments demonstrate that our design with a thickness of approximately 3.27 mm can maintain excellent antireflection performance over a wide angle range of 0 to 45° for both TE and TM waves. Additionally, as a result of adopting low-density substrates (polyethylene terephthalate and polymethylacrylimide foam) and multilayered graphene films, the proposed metasurface shows the advantage of ultralight weight, thus opening an avenue for a number of engineering applications such as electromagnetic shielding, information security, and electromagnetic compatibility technology. In addition, owing to the natural characteristics (corrosion resistance, bending resistance, etc.) of multilayered graphene films, the proposed metasurface shows enormous potential in some particular application scenarios with harsh conditions.

KEYWORDS: broadband scattering suppression, ultrathin, ultralight, multilayered graphene, metasurface
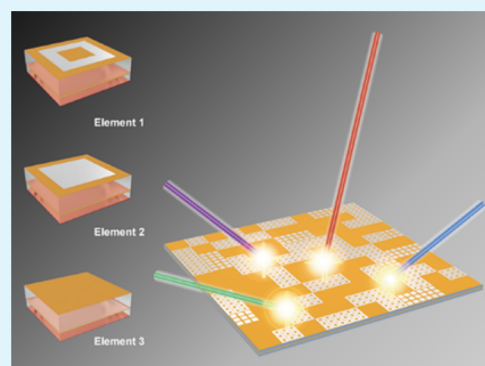
INTRODUCTION

As an ancient research area, microwave absorbers or low reflectors[1−7] have attracted much attention due to their excellent abilities to dissipate or antireflect incident electromagnetic (EM) power and therefore restrain the mirror reflection and transmission of microwaves. To date, such antireflection technologies have been widely used in military fields for several decades, such as in radar cross section (RCS) reduction,[8−11] where low-frequency stealth (Ku band (12−18 GHz), X band (8−12 GHz), and even lower) is urgently needed. Additionally, with the prompt development of fifth-generation (5G) high-speed wireless communication technology, millimeter waves ranging from 24.25 to 43.5 GHz have officially become a hot topic and a recent trend in the study of wireless communication.[12,13] Notably, electromagnetic interference (EMI) and a lack of electromagnetic compatibility (EMC) are inevitable problems that can seriously affect the quality of 5G communication.[14,15] To tackle these problems, millimeter-wave absorbers or antireflectors[16−19] have been employed to improve the isolation among transmitters and/or transceivers. Although numerous studies in the corresponding operation frequency bands have been performed, devising a suitable solution to simultaneously address the abovementioned problems is still in great demand.

To solve these serious problems, two different approaches, including the use of traditional EM absorbers and the use of metamaterials/metasurfaces have been attempted by researchers. With regard to conventional broadband EM absorbers, ferromagnets are always selected and utilized to transform the incident EM energy into heat,[20−24] resulting in a significant reduction in the reflected waves along the echo direction; thus, ferromagnets are widely used in many fields such as EM shielding and anti-EMI. However, the high density and large thickness hinder their use in electronic applications in some unusual scenarios. Currently, metamaterials[25,26] or metasurfaces,[27,28] as an alternative scheme, consist of subwavelength structures and have been proposed to realize many exotic phenomena such as negative refraction,[29,30] EM black holes,[31] holographic imaging,[32,33] and anomalous reflection/transmission,[34,35] providing the possibility of solving this problem. Several attempts have been made to realize broadband low reflection by using metamaterials but with various drawbacks.
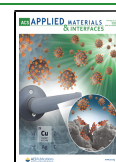
For example, Li et al. proposed a thin-layered metamaterial absorber based on carbonyl iron nanocrystalline flakes with more than 90% absorption (a normal reflectivity of less than 0.1) in 4−40 GHz,[36] but it suffers from the heavy densities of the substrates and the difficulty in the manufacture of standing-up meta-atoms. Song et al.[37] and Zhang et al.[38] proposed three-dimensional (3D) metastructures that can realize self-recoverability and ultrabroad absorption. Nevertheless, the large thickness critically restricts their practical applications. Additionally, the metasurface, as a kind of two-dimensional (2D) metamaterial, has also been used to achieve low backward scattering and spread the reflected energy into various directions by tailoring the spatial profile of low-loss meta-atoms. Despite the thin thickness, most of these metasurfaces either exhibit narrowband absorption or are limited to only one operation band (microwave band or millimeter-wave band).[39,40] Li et al. demonstrated a metasurface Salisbury screen with a subwavelength thickness that can exhibit an efficient absorption of over 89% in an ultrawide frequency band ranging from 4.1 to 17.5 GHz. However, it has no response to millimeter-wave spectra.[41] Therefore, achieving a cross-broadband antireflection metamaterial or metasurface with ultralow density and thin thickness is still challenging.

In this paper, aiming at ultrabroadband low reflection, a multilayered graphene-based metasurface is designed and proposed by utilizing a joint optimization method,[42] in which EM absorption and EM diffusion[43,44] are achieved in the same artificial array, leading to excellent antireflection (a reflectivity of less than 0.1) in a frequency band from 7.5 to 43 GHz, which successfully covers part of the microwave band and part of the millimeter-wave band. With the help of the co-optimization strategy, the operation bandwidth and the scattering suppression ability of the metasurface can be custom-designed as desired, and automated design can even be implemented by utilizing this method. Different from the traditional method to extend the operation bandwidth by superimposing many adjacent resonant modes in a system,[45] only finite resonant modes (a total of four resonances, shown in Figure 2e) are excited by incident EM waves to modulate the distribution of the reflection amplitudes and phases of the proposed meta-atoms. Then, a broadband EM response simultaneously including absorption and backward diffusion is achieved by deliberately arranging these elements across the aperture. The optimized metasurface and the corresponding meta-atoms are modeled in Figure 1 through structural design. Notably, with the aid of polymethylacrylimide (PMI) foam (a density of 50 kg/m³ and a dielectric constant of 1.05 + i0.001) and polyethylene terephthalate (PET) film (a thickness of 0.175 or 0.05 mm, a density of 1380 kg/m³, and a dielectric constant of 2.7 + i0.005), the whole structure is exceptionally lightweight, resulting in excellent application value in engineering. Moreover, graphene has been a promising material for technological applications owing to its remarkable electrical, mechanical, and thermal properties. To date, graphene has illustrated excellent absorption features from terahertz to visible light, ascribed to interband free-carrier transitions or intraband free-carrier dynamics,[46] and the optical absorption performance can be increased by stacking graphene layers.[47] Even though single-layered or few-layered graphene shows some fascinating phenomena, the relatively low conductivity limits its development along with the extreme difficulty in large-area processing. To eliminate these problems, multilayered graphene films are herein synthesized with different
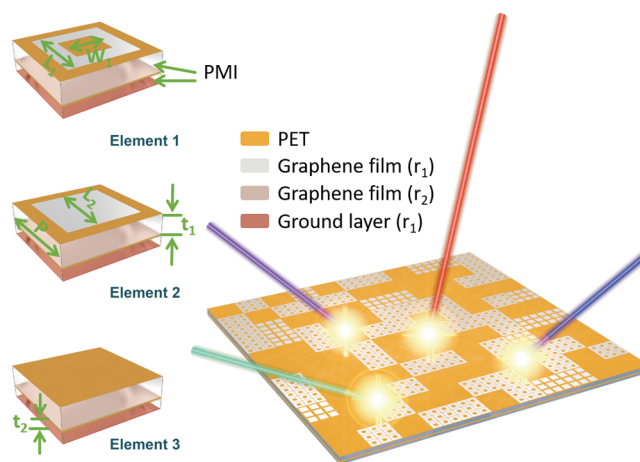
Figure 1. Schematic of the proposed metasurface and corresponding unit cells. Light lines with different colors represent incident waves of different frequencies.

sheet resistances as needed. Note that due to the robust properties of the fabricated multilayered graphene film,[48,49] our design can be improved in the future and may provide a promising way to achieve low reflectors for use in some special application scenarios with extreme environmental impact loads.

■ THEORY AND DESIGN

Based on EM theory, the normal reflectivity (R) from the proposed metasurface can be calculated as

$$R = 20 \log \left| \sum_{i=1}^{n} p_i \times a_i \exp(j\varphi_i) \right| \quad \text{and} \quad \sum_{i=1}^{n} p_i = 1 \tag{1}$$

where p_i, a_i, and φ_i ($i = 1, 2, 3$) are the proportion, reflection amplitude, and reflection phase of the ith type of meta-atom, respectively. According to eq 1, the main factor affecting the total R of the metasurface is the reflection response of each unit cell and the inter-reaction among them. Hence, to minimize the R of the metasurface automatically in an operation band of interest, a co-optimization method (Figure S1a) that combines a commercial simulation tool (CST Microwave Studio) with genetic algorithm (GA) optimization is used to select the proper meta-atoms. (See Supporting Note S1 for a detailed introduction into the joint optimization method.) The final designed low-reflection metasurface is formed by three different elements (Figure 1) with optimized reflection amplitudes and phases. As illustrated in Figure 1, a square-ring-shaped resonator (Element 1) and a patch resonator (Element 2) are observed at the top of the whole structures, while no pattern is discovered in Element 3. (In the following content, the applied graphene refers to multilayered graphene.) All the top patterns hosted by PET layers are made of a graphene film with a sheet resistance r_1 of 0.03 Ω/□. A thin PET film with a thickness of 50 μm is adopted. Additionally, full-layer graphene films with a thickness of 0.175 mm and a sheet resistance r_2 of 141 Ω/□ are located in the middle of the whole structures (Element 1, Element 2, and Element 3) and supported by the PET films. Lossless PMI foam with low density is selected as the substrate to support and link the adjacent layers (Figure 1). The other structural parameters of the proposed elements are provided in Table 1. Simultaneously, the space occupancies p_1 (for Element 1), p_2

Table 1. Optimized Parameters of the Three Basic Elements

| W_1	L_1	W_2	L_2	W_3	L_3	P
2.6 mm	6.0 mm	0 mm	4.8 mm	0 mm	0 mm	6.4 mm
r_1	r_2	t_1	t_2	p_1	p_2	p_3
0.03 Ω/□	141 Ω/□	1.0 mm	2.0 mm	38.0%	11.6%	50.4%

(for Element 2), and p_3 (for Element 3) of each optimized element across the metasurface are also given in Table 1. (See Supporting Note S2 for a detailed introduction into the unit cell and aperture optimization.)

Although suitable units and their space occupancies have been obtained, to realize broadband performance and low reflection, the spatial arrangement of the proposed meta-atoms should also be deliberately designed according to the corresponding element occupancies, as calculated in Table 1. Before optimizing the aperture configuration of the metasurface, we first define 3 × 3 identical meta-atoms as a super element that can maximize the geometrical similarity and mimic the periodic boundary condition. Then, by utilizing the same optimization strategy mentioned in Supporting Note S1, the optimal spatial distribution, as shown in Figures 1 and 3, is finally acquired to suppress the backward scattering to the maximum extent.

To show the performance of the predesigned metasurface, a full-wave simulation is carried out (Figure 2a) to uncover the reflection characteristics by utilizing CST Microwave Studio 2019. From Figure 2a, notably, under illumination with a normal plane wave, a backward reflectivity of less than 0.1 is achieved from 7.5 to 43 GHz, in which the relative bandwidth can reach 140.6%, offering design possibilities for ultra-

broadband EM shielding and compatibility devices. Then, to reveal the physical mechanism of the outstanding performance of the graphene-based metasurface, the reflection responses of the three optimal elements are presented in Figure 2d,e. Considering the use of a lossy conductive material (the middle graphene layer), Element 1 and Element 2 show excellent absorption at both edges of the target waveband, and the absorptivity of Element 3, which gradually increases with frequency, always remains high (Figure 2d). Through the co-contribution of the three lossy meta-atoms, the primary absorption feature of the metasurface can be realized, as shown in Figure 2b, resulting in dissipation of part of the incident energy. Additionally, due to the phase difference among the typical particles (Figure 2e), broadband random diffusion can be achieved based on the generalized Snell's law,[50] thus leading to omnidirectional-like reflection similar to light shining on a rough surface. To further evaluate the contribution of the diffuse scattering to the restraint of the backward reflection, the anomalous scattering energy in the frequency band of 5−45 GHz is also calculated (Figure 2c), and the diffusion phenomenon is found to play an essential role in suppressing the specular reflection from the metasurface upon illumination by normal plane waves.

Since the reflection responses (amplitude and phase) of the elements are mainly due to the resonant feature of the corresponding structures, to obtain further insight into the physical mechanism, the simulated surface currents of the unit cells under normal incidence linearly polarized waves are illustrated (Figure 2f−i). The corresponding resonance frequencies are all marked at the places where abrupt phase shifts occur (Figure 2e). For resonance **R1** in Element 1, two
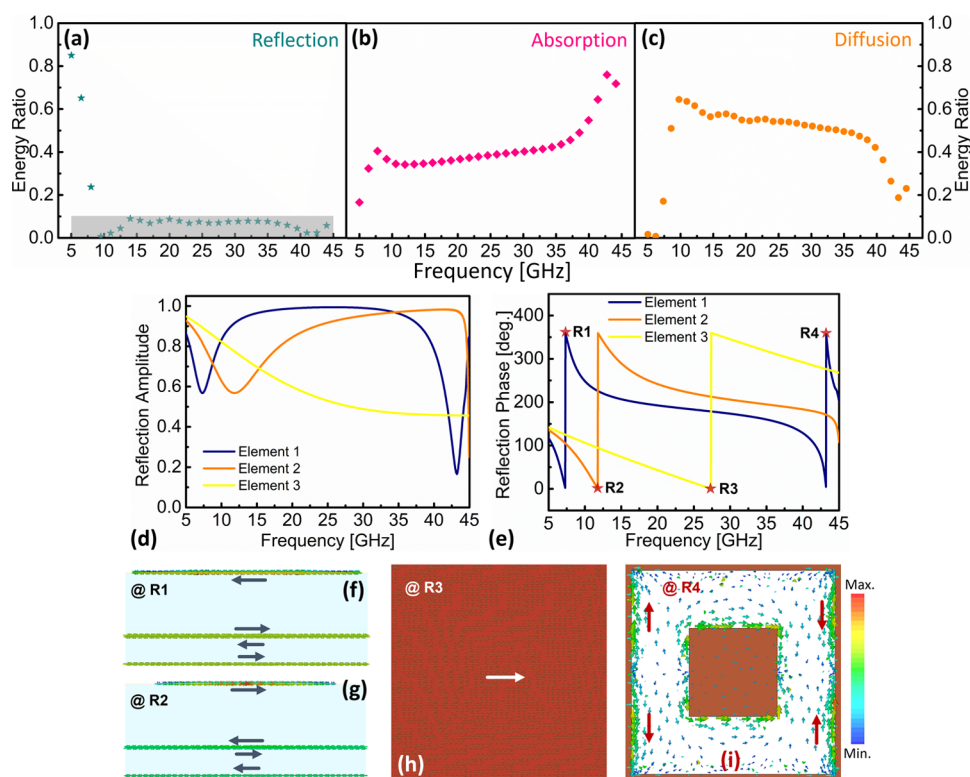
Figure 2. Simulated energy occupation of backward EM waves versus frequency: (a) specular reflection; (b) absorption; (c) diffusion. Simulated reflection amplitudes (d) and phases (e) of the typical unit cells. Simulated surface currents at normal incidence: cross-sectional view at **R1** (f), cross-sectional view at **R2** (g), top view at **R3** (h), and top view at **R4** (i).
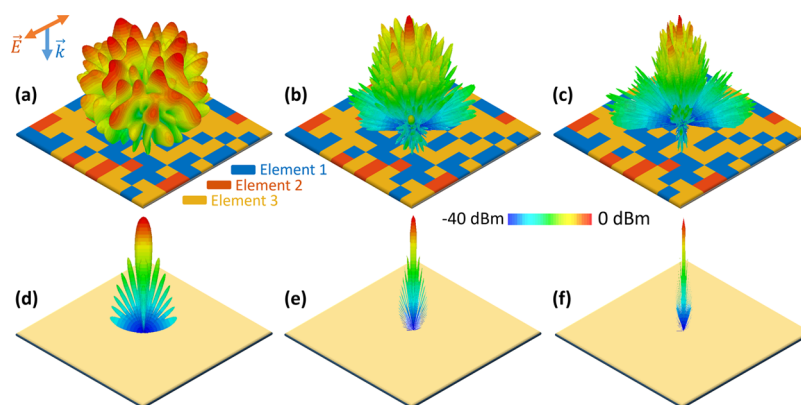
Figure 3. Simulated 3D scattering patterns of the proposed metasurface (a−c) and same-sized metallic plate (d−f) for normal incidence at 10, 25, and 40 GHz.
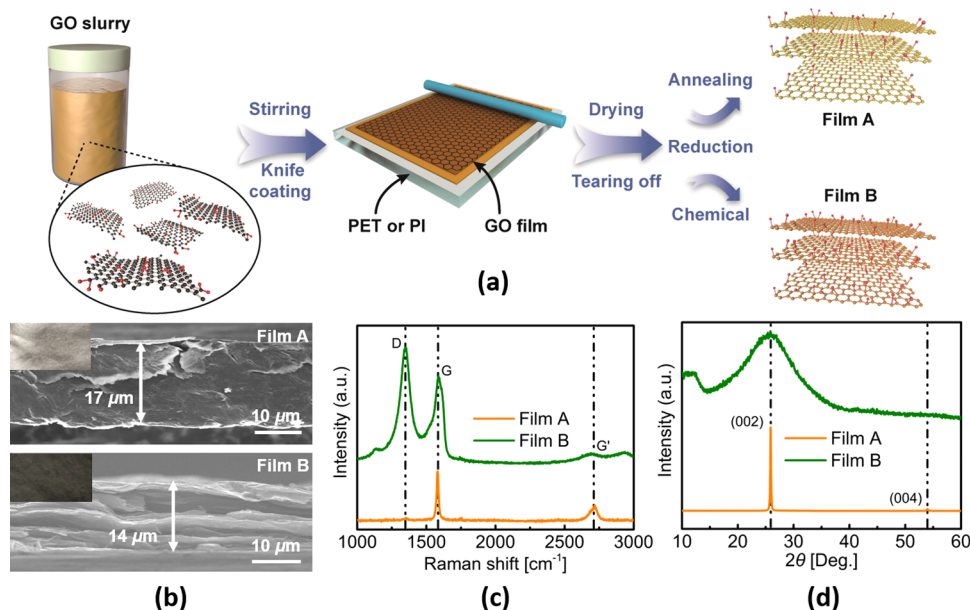
Figure 4. (a) Schematic illustration of the synthesis flow for graphene films with different sheet resistances. SEM images (b), Raman spectra (c), and XRD spectra for Film A and Film B. Insets of panel (b): photographs of Film A and Film B.

sets of antiparallel currents induced by near-field coupling between the top pattern/ground layer and the middle graphene layer can be revealed (Figure 2f), therefore proving the absorption and phase delay originating from the magnetic resonance. Despite the structural difference of the top-layer particles, similar phenomena can also be caused by the magnetic resonance at **R2** in Element 2 (Figure 2g). Figure 2h shows the top view of the simulated surface currents at **R3** in Element 3, and many currents are localized in the middle graphene layer due to the electric resonance, accompanied by a significant ohmic loss at the metasurface. Regarding **R4** in Element 1 (Figure 2i), antiparallel currents are found at the two sides of the top square-ring-shaped structure; that is, the incident waves can drive magnetic resonance between the adjacent meta-atoms. Moreover, because of the lower sheet resistance of the top pattern than of the middle graphene layer, the Q factor at **R4** is higher than those at **R1**, **R2**, and **R3** (Figure 2d).

In the following, to better understand the diffusion effect induced by the lossy metastructures, the 3D scattering patterns are presented in Figure 3a−c for normal incidence waves at 10,

25, and 40 GHz. Additionally, the 3D scattering patterns of a same-sized metallic plate are also provided in Figure 3d−f for comparison with our design (Figure 3a−c). According to the full-wave simulated results (Figure 3a−c), the reflected energy is dispersed in various directions in an ultrabroad frequency range due to the destructive interference from the elementary unit cells with suitable phase differences (Figure 2e).

■ FABRICATION AND MEASUREMENT

Preparation of Graphene Films with Different Sheet Resistances. The graphene films were implemented through the following steps (Figure 4a). First, a graphene oxide (GO) slurry was diluted with ultrapure water to achieve a GO suspension with a 15 mg/mL concentration. Second, the diluted GO suspension was drawn on a PET substrate with a thickness of 0.05 mm. The corresponding GO film was obtained by evaporating the solution and tearing the film off from the substrate. Then, graphene films with different sheet resistances were achieved by two different reduction methods: annealing under an argon atmosphere at 3000 °C for 1 h (Film A) and reduction in 50 mg/mL ascorbic acid aqueous solution

for 2 h (Film B). The sheet resistances of Film A and Film B measured by the four-probe method are 30 ± 1 m$\Omega/\square$ and 141 ± 2 $\Omega/\square$, respectively. Scanning electron microscopy (SEM) images (Figure 4b) show thicknesses for Film A and Film B of 17 and 14 μm. Additionally, from the insets of Figure 4b, Film A has a more pronounced metallic luster than Film B, qualitatively reflecting the high conductivity of Film A. Moreover, the Raman (Figure 4c) and X-ray diffraction (XRD) (Figure 4d) spectra of Film A and Film B were all obtained to verify that the synthesized films were composed of graphene films. The high-temperature annealed Film A had a strong G′ peak and a weak D peak, indicating high-quality graphitization (the orange line in Figure 4c). In contrast, the chemically reduced Film B (the olive line in Figure 4c) showed more defects (a strong D peak) and low graphitization (a weak G′ peak). The strong intensity of the characteristic graphitic (002) peak of Film A located at $2\theta = 26.5°$ (the orange line in Figure 4d) proved that Film A had a stacking structure of graphene sheets. However, Film B with low orientation order had a wide half-width at $2\theta = 26.5°$ (the olive line in Figure 4d), which was consistent with the measured Raman spectral data (Figure 4c).

Fabrication of the Proposed Low-Reflection Metasurface. To verify the correctness of the design method for the proposed ultralight and ultrabroadband graphene-based low-reflection metasurface, a sample was fabricated according to the optimized structural parameters (Table 1) and the aperture configuration (Figures 1 and 3) obtained through the combined optimization method, and a photograph of the sample with 11 × 11 supercells is depicted in Figure 5b. The
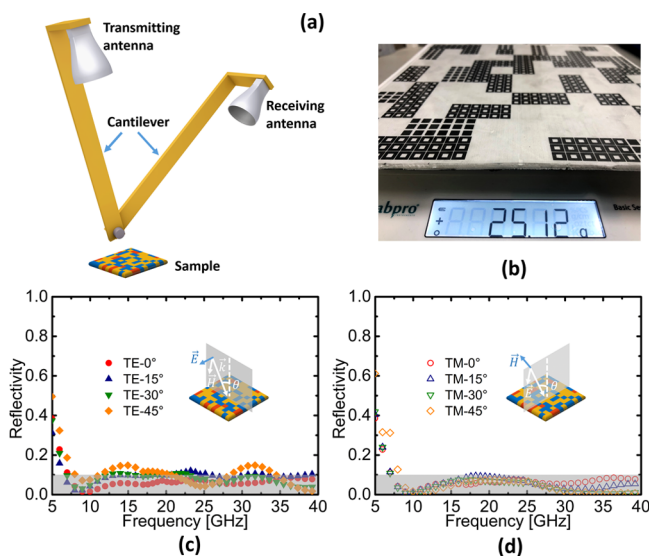
Figure 5. (a) Schematic of the custom-built experimental setup. (b) Photograph of the fabricated sample placed on an electronic balance. Measured reflectivity of the sample illuminated with TE (c) and TM (d) mode plane waves.

laser etching process was adopted to pattern the top-layer graphene film with a processing precision of ± 20 μm. The substrate made of PMI foam was fabricated using computer numerical control (CNC) machine tools with high accuracy. Owing to the low densities of the substrates (PMI foam and PET film) and the graphene films (approximately 1500 kg/m^3), the manufactured sample shows another excellent advantage of light weight primarily of concern in EM absorber

and stealth design, making it relevant to some unique application scenarios. To further exhibit the lightweight property of the proposed metasurface more vividly and graphically, the fabricated sample was weighed using an electronic balance, as shown in Figure 5b, and the corresponding calculated density of 197.1 kg/m^3 (the surface mass density is 0.64 kg/m^2) is only approximately 1/10 the density of FR-4 (1700−1900 kg/m^3) and approximately 1/50 the density of copper (8960 kg/m^3).

Experimental Section. To complete the experimental measurement calibration and measure the normalized broadband reflectivity, an experimental setup (Figure 5a) was built in an anechoic chamber. The adopted test system included a transmission horn antenna, a receiving horn antenna, a vector network analyzer (VNA, N5247A, to 40 GHz), and a cantilever system, as illustrated in Figure 5a. In our experiments, the VNA was used to acquire the response data of the fabricated sample and same-sized metallic plate by obtaining the transmission coefficients ($S21$); therefore, the normalized reflectivity can be calculated by comparing these two $S21$ values. More specifically, the standard gain horn antennas were connected to two ports of the VNA through two low-loss and phase-steady cables. Note that three pairs of different standard gain antennas (operation frequencies: 5−8, 8−18, and 18−40 GHz) were employed to satisfy the test range of 5 to 40 GHz and that due to the limitation of the working frequency of the VNA, which is no more than 40 GHz, the reflection response of the sample exceeding 40 GHz cannot be given here. With the help of the cantilever system, the reflection coefficients of the sample under normal or oblique incidence can be obtained by rotating the cantilevers connected to the corresponding standard gain horn antennas (Figure 5a) by the same angle but in opposite directions synchronously. When conducting the measurement, the antennas were located far enough away from the sample to meet the far-field condition to guarantee the test correctness and accuracy.

RESULTS AND DISCUSSION

To verify the simulated results, the manufactured metasurface was experimentally measured using the custom-built test setup, as shown in Figure 5a. For normal plane wave incidence cases, the reflectivity of the sample was determined (Figure 5c,d), and good agreement between the simulation (Figure 2a) and measurements can be easily observed. Due to the symmetry of the basic unit cells (Figure 1), the measured spectrum of the TE mode (Figure 5c) is in good accordance with that of the TM mode (Figure 5d), providing the polarization-insensitive characteristic. Additionally, the proposed metasurface still exhibits low backward specular reflection from 7.5 to 43 GHz even when the incident angle increases to 45° for both the TE and TM cases, manifesting excellent angular robustness (Figure 5c,d). The verified ultralightweight and ultrabroadband low-reflection features of the thin-thickness graphene-based metasurface make it an eligible candidate for real-world applications.

CONCLUSIONS

In this paper, a graphene-based multilayer metasurface (Figure 1) has been investigated to achieve ultrabroadband low reflection with the aid of the joint optimization method, and 90% of the backward reflected energy can be suppressed by our

design in the whole band of 7.5 to 43 GHz under normal incidence. Two mechanisms, absorption and backward diffusion, are employed to compensate for each other to achieve ultrabroadband RCS reduction with thin thickness and light weight. Such compensation also gives rise to excellent angular stability below 45°. A prototype of the proposed metasurface was fabricated (Figure 5b), and the measurement results (Figure 5c,d) are in good agreement with the numerical results (Figure 2a). In addition, the performance of the manufactured sample remains stable as the incident angle increases from 0 to 45° for both the TE and TM polarizations (Figure 5c,d). Combining the extraordinarily ultralight features of the graphene film and PMI foam, our proposed design offers an ultralow density, providing the possibility of realizing lightness of structural devices. Moreover, the graphene film also natively provides a low-reflection metasurface with the potential characteristics of robust flexibility, corrosion resistance, salt-fog resistance, and anti-high temperature. We remark that the proposed thin-thickness design is of great practical significance and engineering value, and it can be used to realize anti-EMI, EMC, and stealth for both civil and military applications.

■ ASSOCIATED CONTENT

ⓈI Supporting Information

The Supporting Information is available free of charge at https://pubs.acs.org/doi/10.1021/acsami.0c20499.

> Detailed introduction into the joint optimization method; detailed introduction into unit cell and aperture optimization (PDF)

■ AUTHOR INFORMATION

Corresponding Authors

Cheng Zhang − *Hubei Engineering Research Center of RF-Microwave Technology and Application, School of Science, Wuhan University of Technology, Wuhan 430070, China;* ⓞ orcid.org/0000-0002-8948-4093; Email: czhang2020@whut.edu.cn

Da Ping He − *Hubei Engineering Research Center of RF-Microwave Technology and Application, School of Science and State Key Laboratory of Advanced Technology for Materials Synthesis and Processing, Wuhan University of Technology, Wuhan 430070, China;* ⓞ orcid.org/0000-0002-0284-4990; Email: hedaping@whut.edu.cn

Qiang Cheng − *Department of Radio Engineering, State Key Laboratory of Millimeter Waves, Southeast University, Nanjing 210096, China;* Email: qiangcheng@seu.edu.cn

Authors

Jie Zhao − *Department of Radio Engineering, State Key Laboratory of Millimeter Waves, Southeast University, Nanjing 210096, China*

Bo Han Zhang − *Hubei Engineering Research Center of RF-Microwave Technology and Application, School of Science and School of Information Engineering, Wuhan University of Technology, Wuhan 430070, China*

Rong Guo Song − *Hubei Engineering Research Center of RF-Microwave Technology and Application, School of Science and School of Information Engineering, Wuhan University of Technology, Wuhan 430070, China*

Yu Chao Wang − *Hubei Engineering Research Center of RF-Microwave Technology and Application, School of Science, Wuhan University of Technology, Wuhan 430070, China*

Complete contact information is available at:
https://pubs.acs.org/10.1021/acsami.0c20499

Author Contributions

&C.Z. and J.Z. contributed equally to this work.

Notes

The authors declare no competing financial interest.

■ ACKNOWLEDGMENTS

■ REFERENCES

(1) Musal, H. M.; Hahn, H. T. Thin-Layer Electromagnetic Absorber Design. *IEEE Trans. Magn.* **1989**, *25*, 3851−3853.

(2) Luukkonen, O.; Costa, F.; Simovski, C. R.; Monorchio, A.; Tretyakov, S. A. A Thin Electromagnetic Absorber for Wide Incidence Angles and Both Polarizations. *IEEE Trans. Antennas Propag.* **2009**, *57*, 3119−3125.

(3) Lv, H.; Guo, Y.; Zhao, Y.; Zhang, H.; Zhang, B.; Ji, G.; Xu, J. Z. Achieving Tunable Electromagnetic Absorber via Graphene/Carbon Sphere Composites. *Carbon* **2016**, *110*, 130−137.

(4) Lv, H.; Yang, Z.; Ong, S. J. H.; Wei, C.; Liao, H.; Xi, S.; Du, Y.; Ji, G.; Xu, Z. J. A Flexible Microwave Shield with Tunable Frequency-Transmission and Electromagnetic Compatibility. *Adv. Funct. Mater.* **2019**, *29*, 1900163.

(5) Holloway, C. L.; DeLyser, R. R.; German, R. F.; McKenna, P.; Kanda, M. Comparison of Electromagnetic Absorber Used in Anechoic and Semi-Anechoic Chambers for Emissions and Immunity Testing of Digital Devices. *IEEE Trans. Electromagn. Compat.* **1997**, *39*, 33−47.

(6) Xu, Y.; Yang, Y.; Yan, D. X.; Duan, H.; Zhao, G.; Liu, Y. Gradient Structure Design of Flexible Waterborne Polyurethane Conductive Films for Ultraefficient Electromagnetic Shielding with Low Reflection Characteristic. *ACS Appl. Mater. Interfaces* **2018**, *10*, 19143−19152.

(7) Wang, Y.; Wang, W.; Ding, X.; Yu, D. Multilayer-Structured Ni-Co-Fe-P/Polyaniline/Polyimide Composite Fabric for Robust Electromagnetic Shielding with Low Reflection Characteristic. *Chem. Eng. J.* **2020**, *380*, 122553.

(8) Knott, E.; Shaeffer, J. F.; Tuley, M. T. *Radar Cross Section*, 2nd ed.; Artech House: Boston, 1993.

(9) Edalati, A.; Sarabandi, K. Wideband, Wide Angle, Polarization Independent RCS Reduction Using Nonabsorptive Miniaturized-Element Frequency Selective Surfaces. *IEEE Trans. Antennas Propag.* **2014**, *62*, 747−754.

(10) Liu, T.; Cao, X.; Gao, J.; Zheng, Q.; Li, W.; Yang, H. RCS Reduction of Waveguide Slot Antenna with Metamaterial Absorber. *IEEE Trans. Antennas Propag.* **2013**, *61*, 1479−1484.

(11) Jia, Y.; Liu, Y.; Guo, Y. J.; Li, K.; Gong, S. X. Broadband Polarization Rotation Reflective Surfaces and Their Applications to RCS Reduction. *IEEE Trans. Antennas Propag.* **2016**, *64*, 179−188.

(12) Rappaport, T. S.; Xing, Y.; MacCartney, G. R.; Molisch, A. F.; Mellios, E.; Zhang, J. Overview of Millimeter Wave Communications for Fifth-Generation (5G) Wireless Networks—With a Focus on

Propagation Models. *IEEE Trans. Antennas Propag.* **2017**, *65*, 6213−6230.

(13) Sharma, P. Evolution of Mobile Wireless Communication Networks-1G to 5G as well as Future Prospective of Next Generation Communication Network. *Int. J. Comput. Sci. Mobile Comput.* **2013**, *2*, 47−53.

(14) Tirkey, M. M.; Gupta, N. Electromagnetic Absorber Design Challenges. *IEEE Electromagn. Compat. Mag.* **2019**, *8*, 59−65.

(15) Alsharif, M. H.; Nordin, R. Evolution towards Fifth Generation (5G) Wireless Networks: Current Trends and Challenges in the Deployment of Millimetre Wave Massive MIMO and Small Cells. *Telecommun. Syst.* **2016**, *64*, 617−637.

(16) Joseph, N.; Varghese, J.; Sebastian, M. T. In Situ Polymerized Polyaniline Nanofiber-Based Functional Cotton and Nylon Fabrics as Millimeter-Wave Absorbers. *Polym. J.* **2017**, *49*, 391−399.

(17) Namai, A.; Sakurai, S.; Nakajima, M.; Suemoto, T.; Matsumoto, K.; Goto, M.; Sasaki, S.; Ohkoshi, S. I. Synthesis of an Electromagnetic Wave Absorber for High-Speed Wireless Communication. *J. Am. Chem. Soc.* **2009**, *131*, 1170−1173.

(18) Zhang, C.; Yang, J.; Cao, W.; Yuan, W.; Ke, J.; Yang, L.; Cheng, Q.; Cui, T. Transparently Curved Metamaterial with Broadband Millimeter Wave Absorption. *Photonics Res.* **2019**, *7*, 478−485.

(19) Wu, B.; Tuncer, H. M.; Naeem, M.; Yang, B.; Cole, M. T.; Milne, W. I.; Hao, Y. Experimental Demonstration of a Transparent Graphene Millimeter Wave Absorber with 28% Fractional Bandwidth at 140 GHz. *Sci. Rep.* **2014**, *4*, 4130.

(20) Naito, Y.; Suetake, K. Application of Ferrite to Electromagnetic Wave Absorber and its Characteristics. *IEEE Trans. Microwave Theory Tech.* **1971**, *19*, 65−72.

(21) Ohkoshi, S.; Kuroki, S.; Sakurai, S.; Matsumoto, K.; Sato, K.; Sasaki, S. A Millimeter-Wave Absorber Based on Gallium-Substituted ε-Iron Oxide Nanomagnets. *Angew. Chem., Int. Ed.* **2007**, *46*, 8392−8395.

(22) Namai, A.; Kurahashi, S.; Hachiya, H.; Tomita, K.; Sakurai, S.; Matsumoto, K.; Goto, Y.; Ohkoshi, S. High Magnetic Permeability of ε-Ga$_x$Fe$_{2-x}$O$_3$ Magnets in the Millimeter Wave Region. *J. Appl. Phys.* **2010**, *107*, 09A955/1−09A955/3.

(23) Wu, G.; Zhang, H.; Luo, X.; Yang, L.; Lv, H. Investigation and Optimization of Fe/ZnFe2O4 as a Wide-Band Electromagnetic Absorber. *J. Colloid Interface Sci.* **2019**, *536*, 548−555.

(24) Wang, Y.; Gao, X.; Zhang, L.; Wu, X.; Wang, Q.; Luo, C.; Wu, G. Synthesis of Ti3C2/Fe3O4/PANI Hierarchical Architecture Composite as an Efficient Wide-Band Electromagnetic Absorber. *Appl. Surf. Sci.* **2019**, *480*, 830−838.

(25) Cui, T. J. Microwave Metamaterials. *Nat. Sci. Rev.* **2017**, *5*, 134−136.

(26) Cui, T. J. Microwave Metamaterials—from Passive to Digital and Programmable Controls of Electromagnetic Waves. *J. Opt.* **2017**, *19*, No. 084004.

(27) Yu, N.; Capasso, F. Flat Optics with Designer Metasurfaces. *Nature Mater.* **2014**, *13*, 139−150.

(28) Estakhri, N. M.; Alù, A. Wave-Front Transformation with Gradient Metasurfaces. *Phys. Rev. X* **2016**, *6*, 041008.

(29) Smith, D. R.; Pendry, J. B.; Witshire, M. C. Metamaterials and Negative Refractive Index. *Science* **2004**, *305*, 788−792.

(30) Shelby, R. A.; Smith, D. R.; Schultz, S. Experimental Verification of a Negative Index of Refraction. *Science* **2001**, *292*, 77−79.

(31) Cheng, Q.; Cui, T. J.; Jiang, W. X.; Cai, B. G. An Omnidirectional Electromagnetic Absorber Made of Metamaterials. *New J. Phys.* **2010**, *12*, No. 063006.

(32) Zheng, G.; Mühlenbernd, H.; Kenney, M.; Li, G.; Zentgraf, T.; Zhang, S. Metasurface Holograms Reaching 80% Efficiency. *Nat. Nanotechnol.* **2015**, *10*, 308−312.

(33) Li, L.; Cui, T. J.; Ji, W.; Liu, S.; Ding, J.; Wan, X.; Li, Y. B.; Jiang, M.; Qiu, C. W.; Zhang, S. Electromagnetic Reprogrammable Coding-Metasurface Holograms. *Nat. Commun.* **2017**, *8*, 197.

(34) Dong, D. S.; Yang, J.; Cheng, Q.; Zhao, J.; Gao, L. H.; Ma, S. J.; Liu, S.; Chen, H. B.; He, Q.; Liu, W. W.; Fang, Z.; Zhou, L.; Cui, T. J.

Teraherz Broadband Low-Reflection Metasurface by Controlling Phase Distributions. *Adv. Opt. Mater.* **2015**, *3*, 1405−1410.

(35) Zhao, J.; Cheng, Q.; Wang, X. K.; Yuan, M. J.; Zhou, X.; Fu, X. J.; Qi, M. Q.; Liu, S.; Chen, H. B.; Zhang, Y.; Cui, T. J. Controlling the Bandwidth of Terahertz Low-Scattering Metasurfaces. *Adv. Opt. Mater.* **2016**, *4*, 1773.

(36) Li, W.; Wu, T.; Wang, W.; Zhai, P.; Guan, J. Broadband Patterned Magnetic Microwave Absorber. *J. Appl. Phys.* **2014**, *116*, No. 044110.

(37) Song, W. L.; Zhou, Z.; Wang, L. C.; Cheng, X. D.; Chen, M.; He, R.; Chen, H.; Yang, Y.; Fang, D. Constructing Repairable Meta-Structures of Ultra-Broad-Band Electromagnetic Absorption from Three-Dimensional Printed Patterned Shells. *ACS Appl. Mater. Interfaces* **2017**, *9*, 43179−43187.

(38) Zhang, K.-L.; Zhang, J. Y.; Hou, Z. L.; Song, B.; Zhao, Q. L. Multifunctional Broadband Microwave Absorption of Flexible Graphene Composites. *Carbon* **2019**, *141*, 608−617.

(39) Zhang, C.; Yang, J.; Yuan, W.; Zhao, J.; Dai, J. Y.; Guo, T. C.; Liang, J.; Xu, G. Y.; Cheng, Q.; Cui, T. J. An Ultralight and Thin Metasurface for Radar-Infrared Bi-Stealth Applications. *J. Phys. D: Appl. Phys.* **2017**, *50*, 444002.

(40) Zhang, C.; Cheng, Q.; Yang, J.; Zhao, J.; Cui, T. J. Broadband Metamaterial for Optical Transparency and Microwave Absorption. *Appl. Phys. Lett.* **2017**, *110*, 143511.

(41) Li, T.; Chen, K.; Ding, G.; Zhao, J.; Jiang, T.; Feng, Y. Optically Transparent Metasurface Salisbury Screen with Wideband Microwave Absorption. *Opt. Express* **2018**, *26*, 34384−34395.

(42) Zhao, J.; Zhang, C.; Cheng, Q.; Yang, J.; Cui, T. J. An Optically Transparent Metasurface for Broadband Microwave Antireflection. *Appl. Phys. Lett.* **2018**, *112*, No. 073504.

(43) Gao, L. H.; Cheng, Q.; Yang, J.; Ma, S. J.; Zhao, J.; Liu, S.; Chen, H. B.; He, Q.; Jiang, W. X.; Ma, H. F.; Wen, Q. Y.; Liang, L. J.; Jin, B. B.; Liu, W. W.; Zhou, L.; Yao, J. Q.; Wu, P. H.; Cui, T. J. Broadband Diffusion of Terahertz Waves by Multi-Bit Coding Metasurfaces. *Light: Sci. Appl.* **2015**, *4*, 324.

(44) Zhang, C.; Song, G. Y.; Ma, H. F.; Yang, J.; Cao, W. K.; Xie, X. Y.; Chen, P.; Cheng, Q.; Wu, L. T.; Cui, T. J. A Metamaterial Route to Realize Acoustic Insulation and Anisotropic Electromagnetic Manipulation Simultaneously. *Adv. Mater. Technol.* **2018**, *3*, 1800161.

(45) Fan, R. H.; Xiong, B.; Peng, R. W.; Wang, M. Constructing Metastructures with Broadband Electromagnetic Functionality. *Adv. Mater.* **2020**, *32*, 1904646.

(46) Hafez, H. A.; Chai, X.; Sekine, Y.; Takamura, M.; Oguri, K.; Al-Naib, I.; Dignam, M. M.; Hibino, H.; Ozaki, T. Effects of Environmental Conditions on the Ultrafast Carrier Dynamics in Graphene Revealed by Terahertz Spectroscopy. *Phys. Rev. B* **2017**, *95*, 165428.

(47) Zhu, Y.; Wang, J.; Peng, R. W.; Wu, S.; Qi, D.; Bao, W.; Liu, L.; Zhu, Y.; Jing, H.; Wang, M. Excitation Enhancement of Hot Electrons by Ultrafast Optical Pumping in Heavily *p*-Doped Graphene Stacks. *Phys. Rev. Applied* **2020**, *14*, No. 064049.

(48) Li, P.; Wang, Z.; Song, R.; Qian, W.; Wen, P.; Yang, Z.; He, D. Customizable Fabrication for Auxetic Graphene Assembled Macrofilms with High Conductivity and Flexibility. *Carbon* **2020**, *162*, 545−551.

(49) Allen, M. J.; Tung, V. C.; Kaner, R. B. Honeycomb Carbon: A Review of Graphene. *Chem. Rev.* **2010**, *110*, 132−145.

(50) Yu, N.; Genevet, P.; Kats, M. A.; Aieta, F.; Tetienne, J. P.; Capasso, F.; Gaburro, Z. Light Propagation with Phase Discontinuities: Generalized Laws of Reflection and Refraction. *Science* **2011**, *334*, 333−337.